

Multi-wavelength bispectrum speckle interferometry of R Cas and comparison of the observations with Mira star models^{*}

K.-H. Hofmann¹, Y. Balega², M. Scholz³, and G. Weigelt¹

¹ Max-Planck-Institut für Radioastronomie, Auf dem Hügel 69, 53121 Bonn, Germany

² Special Astrophysical Observatory, Nizhnij Arkhyz, Zelenchuk region, Karachai-Cherkesia, 357147, Russia

³ Institut für Theoretische Astrophysik der Universität Heidelberg, Tiergartenstrasse 15, 69121 Heidelberg, Germany

Received 18 June 1999 / Accepted 5 November 1999

Abstract. We present diffraction-limited (30 mas) bispectrum speckle interferometry observations of the Mira star R Cas with the Russian 6 m SAO telescope. The speckle interferograms were recorded through narrow-band interference filters with centre wavelength/bandwidth of 671 nm/6 nm and 714 nm/6 nm (strong TiO absorption band), 700 nm/6 nm (moderate TiO absorption), and 1045 nm/9 nm (continuum). The reconstructed images show that the average uniform-disk diameters of R Cas are $43.6 \text{ mas} \pm 2.0 \text{ mas}$ at 671 nm, $49.2 \text{ mas} \pm 2.0 \text{ mas}$ at 714 nm, $37.2 \text{ mas} \pm 2.0 \text{ mas}$ at 700 nm, and $29.9 \text{ mas} \pm 3.0 \text{ mas}$ at 1045 nm. In the 671 nm, 714 nm and 700 nm images the disks of R Cas are non-uniform and elongated with position angles of the long axis of 52° , 57° and 54° , and axis ratios of 0.70, 0.76 and 0.87, respectively. For example, at 671 nm the size (elliptical uniform disk fit) of the elongated R Cas disk is $51.0 \text{ mas} \times 35.6 \text{ mas}$. The 1045 nm image shows no significant asymmetry.

We compare our observations with theoretical Mira star models and systematically check the capacity of monochromatic diameter ratios and linear diameters for discriminating between model representations of the observed star. Monochromatic $\tau_\lambda=1$ radii were derived from the observed visibilities by application of model-predicted center-to-limb variations of the intensity. Adopting the HIPPARCOS parallax we obtained a photospheric radius (Rosseland $\tau_{\text{Ross}}=1$ radius) of R Cas of $377 R_\odot \pm 60 R_\odot$ ($32.9 \text{ mas} \pm 3.3 \text{ mas}$). The derived photospheric radius and the large period (~ 430 days) suggest first overtone pulsation for R Cas. We also determined the effective temperature of R Cas at near-minimum phase to $1880 \text{ K} \pm 130 \text{ K}$ and propose $T_{\text{eff}} \sim 1900 \text{ K}$ for spectral type M10 in the temperature calibration of very late M giant spectral classes.

Key words: techniques: interferometric – methods: observational – stars: imaging – stars: late-type – stars: variables: general – stars: individual: R Cas

Send offprint requests to: K.-H. Hofmann
(hofmann@mpifr-bonn.mpg.de)

^{*} Based on observations collected at the SAO 6 m telescope in Russia

1. Introduction

The resolution of large optical telescopes and interferometers is high enough to resolve the stellar disk of nearby M giant stars, to reveal photospheric asymmetries and surface inhomogeneities, and to study the wavelength, variability phase, and cycle dependence of the diameter (see, e.g., Pease 1931; Bonneau & Labeyrie 1973; Labeyrie et al. 1977; Bonneau et al. 1982; Karovska et al. 1991; Haniff et al. 1992; Quirrenbach et al. 1992; Wilson et al. 1992; Tuthill et al. 1994; Haniff et al. 1995; Hofmann et al. 1995a; Weigelt et al. 1996; Van Belle et al. 1996; Perrin et al. 1999). In strong TiO absorption bands, the diameter of M-type Mira variables is much larger than in the continuum (see the pioneering work of Labeyrie et al. 1977; Bonneau et al. 1982). Theoretical studies (e.g. Watanabe & Kodaira 1979; Scholz 1985; Bessell et al. 1989; Bessell et al. 1996=BSW96) show that accurate monochromatic diameter measurements can improve our understanding of M giant atmospheres.

The first interferometric observations of R Cas at optical wavelengths were reported by Tuthill et al. (1994), Haniff et al. (1995), Hofmann et al. (1995a), Weigelt et al. (1996) and Van Belle et al. (1996). In this paper we present diffraction-limited 6 m telescope bispectrum speckle interferometry images of the Mira variable R Cas. Images with ~ 30 mas resolution were obtained in the 700 nm moderate TiO absorption band, and in the 714 nm and 671 nm strong TiO absorption band. Observations with 54 mas resolution were achieved in the 1045 nm continuum.

2. Observations and data reduction

2.1. Observational parameters

The R Cas speckle interferograms were obtained with the Russian 6 m telescope at the Special Astrophysical Observatory on September 20, 1994, September 30 and October 3, 1996 (see Table 1). The data were recorded through narrow-band interference filters with centre wavelength (nm)/bandwidth (nm) of 671/6, 700/6, 714/6 and 1045/9 (filter width of the 4 filters at 10% transmission level: 9 nm, 9 nm, 8 nm, 13 nm; 1% level: 14 nm, 14 nm, 12 nm, 19 nm, respectively). A typical speckle interferogram of the 1045 nm data is shown in Fig. 1.

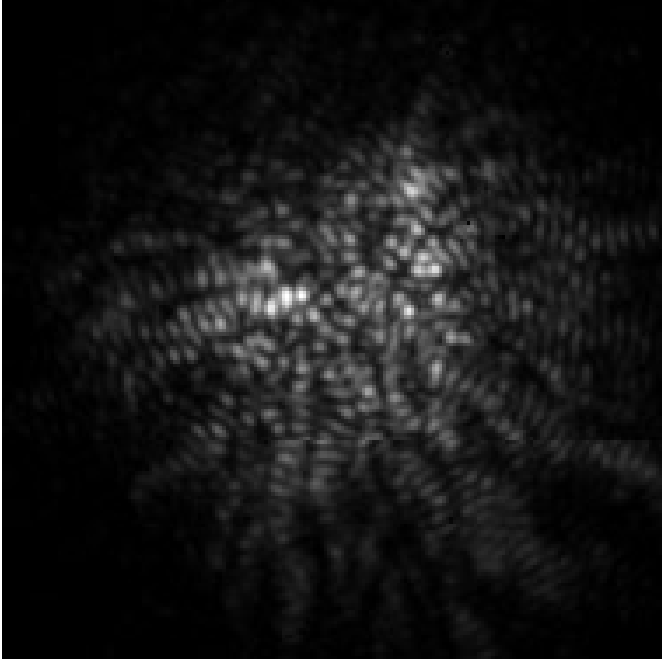


Fig. 1. One of 991 6 m-speckle interferograms of R Cas taken through the 1045 nm/9 nm filter with our NICMOS-3 IR camera. The field of view is $2''.77 \times 2''.77$.

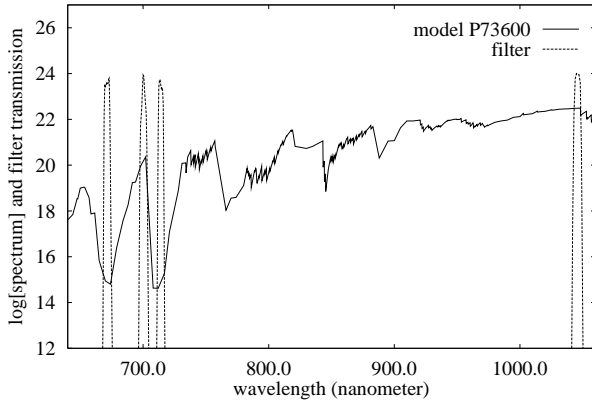


Fig. 2. Model-predicted Mira star spectrum L_ν ($\text{erg s}^{-1} \text{Hz}^{-1}$) together with the transmission curves of our four filters (671 nm/6 nm, 700 nm/6 nm, 714 nm/6 nm and 1045 nm/9 nm).

Fig. 2 shows the transmission curves of the filters. Due to the narrow bandwidth and rectangle-shaped transmission curve of our filters specific areas of the molecular band structure of the Mira star spectrum can be selected which is important for sound physical interpretation (cf. Hofmann & Scholz 1998 = HS98; Hofmann et al. 1998 = HSW98). With these narrow-band filters quasi-monochromatic radii of R Cas can be measured in the strong TiO absorption bands at 671 nm and 714 nm, at the moderate TiO absorption band at 700 nm, and in the continuum at 1045 nm, suited for the comparison with predictions of Mira star models.

Speckle interferograms of the unresolved stars 51 And and HIC 115022 were taken for the calibration of the speckle transfer

Table 1. Observational parameters.

	671 nm, 700 nm and 714 nm filter	1045 nm filter
Epoche	1994.72	1996.75, 1996.76
Variability phase	0.91	0.63
Exp. time/frame	10 ms	50 ms, 20 ms
Number of frames	842; 981; 1592	517, 474
Seeing (FWHM)	1''0	1''9, 1''4
Field of view	2''54	3''74
Pixel size	4.97 mas	14.60 mas

function. The observational parameters are listed in Table 1. The plate scale error is $\pm 1.5\%$ and the error of detector orientation $\pm 0.7^\circ$ (derived from speckle observations of calibration binaries). The optical speckle interferograms were recorded with the speckle camera described by Baier & Weigelt (1983). The detector used was an image intensifier (gain 500 000, quantum efficiency at 656 nm about 8%) coupled optically to a fast CCD camera (512^2 pixels/frame, frame rate 4 frames/s, digital correlated double sampling). The near-infrared speckle raw data (1045 nm continuum) were recorded with our NICMOS-3 camera.

2.2. Diffraction-limited images and visibilities

Diffraction-limited images were reconstructed from the speckle interferograms using the bispectrum speckle interferometry method (Weigelt 1977; Lohmann et al. 1983; Hofmann & Weigelt 1986). The visibility of R Cas was determined with the speckle interferometry method (Labeyrie 1970). The image processing steps applied are described in Hofmann et al. (1995b). The speckle transfer function was derived from speckle interferograms of unresolved stars (51 And and HIC 115022). The correct speckle transfer function was determined by comparison of the object-independent spectral ratio function (Von der L uhe 1984) of object and reference star. The bispectrum of each frame consisted of ~ 37 million elements.

Fig. 3 presents the reconstructed diffraction-limited R Cas images and for comparison the 700 nm reconstruction of the unresolved star 51 And (the speckle transfer function of the 51 And measurement was compensated with the unresolved star γ Ori).

From the reconstructed diffraction-limited visibilities (Figs. 4 and 5) we derived the disk parameters of R Cas by fitting artificial, i.e. non-physical, center-to-limb variations (=CLV) of emitted intensity: uniform disk (UD), fully darkened disk (FDD) and Gaussian function. Because of the clearly visible elongation at optical wavelengths (see Fig. 3), *two-dimensional elliptical* CLV fit functions (elliptical UD, FDD, Gauss) were generated and the length of the long and short axis and the position angle of the long axis were fitted.

Fig. 4 shows azimuthally averaged visibilities at 671 nm, 714 nm and 700 nm together with the azimuthally averaged visibilities of the fitted *two-dimensional elliptical* uniform disk

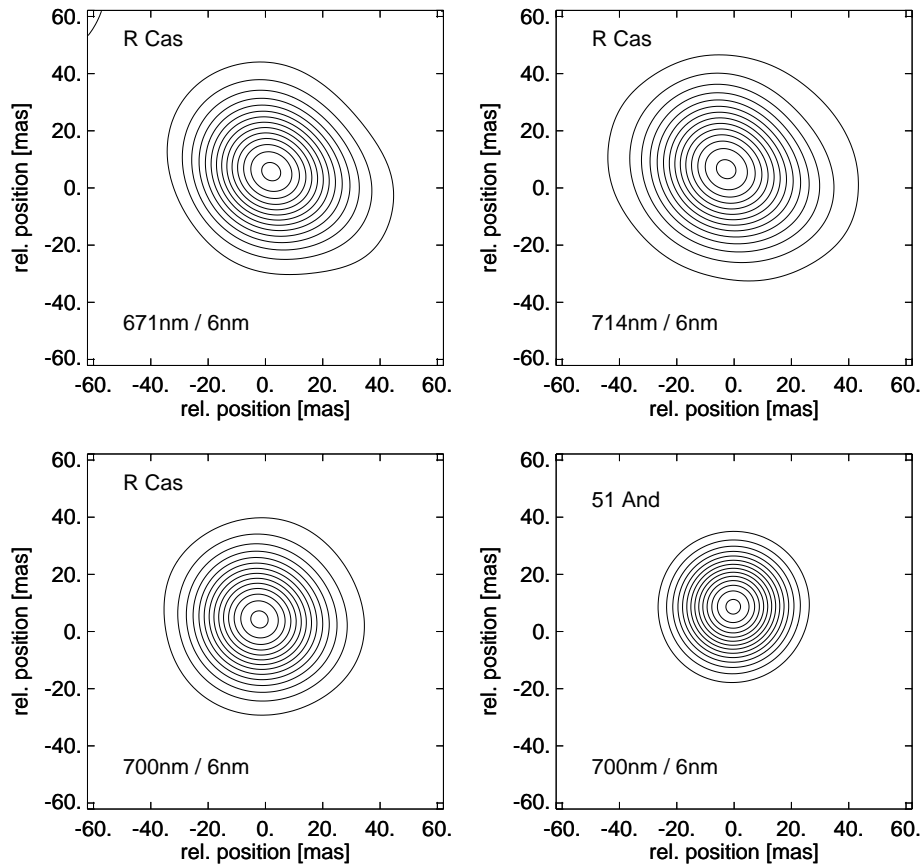


Fig. 3. 30 mas resolution bispectrum speckle interferometry images of R Cas at 671 nm, 714 nm and 700 nm, and for comparison of the unresolved star 51 And at 700 nm. In each panel the contour levels are plotted from 7–98% of peak intensity in steps of 7%. North is at the top and east to the left.

Table 2. Disk parameters derived from fits of artificial CLV (UD, FDD and Gaussian) to the visibilities of R Cas. The determined star disk parameters are (a) the azimuthally averaged uniform-disk (UD) and fully darkened-disk (FDD) diameter, and Gaussian FWHM, (b) the length of major and minor axis of the disk and (c) its position angle, and (d) the axial ratio (minor/major axis).

Data set	Av. diameter/FWHM (mas)	Major axis (mas)	Minor axis (mas)	position angle ($^{\circ}$)	Axis ratio
UD					
671/6	43.6 ± 2.0	51.0 ± 2.4	35.6 ± 2.4	52.4 ± 7.0	0.70 ± 0.07
700/6	37.2 ± 2.0	39.8 ± 2.4	34.6 ± 2.4	54.3 ± 7.0	0.87 ± 0.10
714/6	49.2 ± 2.0	55.6 ± 2.4	42.2 ± 2.4	57.9 ± 7.0	0.76 ± 0.07
1045/9	29.9 ± 3.0	–	–	–	> 0.9
Gaussian					
671/6	27.3 ± 1.4	31.7 ± 1.6	22.4 ± 1.6	52.7 ± 7.0	0.71 ± 0.07
700/6	23.5 ± 1.4	25.1 ± 1.6	21.9 ± 1.6	54.3 ± 7.0	0.87 ± 0.10
714/6	30.8 ± 1.4	34.8 ± 1.6	26.4 ± 1.6	57.2 ± 7.0	0.76 ± 0.07
1045/9	18.5 ± 1.9	–	–	–	> 0.9
FDD					
671/6	49.2 ± 2.2	57.3 ± 2.8	40.2 ± 2.8	52.4 ± 7.0	0.70 ± 0.07
700/6	42.0 ± 2.2	44.9 ± 2.8	39.1 ± 2.8	54.2 ± 7.0	0.87 ± 0.10
714/6	55.4 ± 2.2	62.6 ± 2.8	47.5 ± 2.8	57.7 ± 7.0	0.76 ± 0.07
1045/9	33.3 ± 3.2	–	–	–	> 0.9

and Gaussian functions. Fig. 4 bottom is the azimuthally averaged visibility of the unresolved star 51 And reconstructed in the same way as the R Cas visibilities. Fig. 5 (top) shows the azimuthally averaged visibility of R Cas and of the unresolved star HIC 115022 at 1045 nm together with the UD and Gaussian fit functions. Note, that the Gaussian function fits the re-

constructed visibilities at optical wavelengths much better than FDD and UD, and that all three artificial CLVs fit the 1045 nm visibility equally well. The value of the UD visibility curves at the first minimum is larger than zero since the curves are azimuthal averages of *elliptical* uniform disks (see Fig. 4). Table 2 lists the fitted disk parameters of R Cas. Table 3 contains

Table 3. Linear UD and FDD radii and Gaussian HWHM (in R_{\odot}) based on the HIPPARCOS parallax of R Cas.

Data set	Av. radius	Major axis	Minor axis
UD			
671/6	500 \pm 63	585 \pm 74	408 \pm 55
700/6	427 \pm 55	456 \pm 60	397 \pm 54
714/6	564 \pm 70	638 \pm 80	484 \pm 63
1045/9	343 \pm 53	–	–
Gaussian			
671/6	313 \pm 40	364 \pm 46	257 \pm 35
700/6	269 \pm 35	288 \pm 38	251 \pm 35
714/6	353 \pm 44	399 \pm 50	303 \pm 40
1045/9	212 \pm 33	–	–
FDD			
671/6	564 \pm 71	657 \pm 84	461 \pm 63
700/6	482 \pm 62	515 \pm 68	448 \pm 62
714/6	635 \pm 79	718 \pm 90	545 \pm 72
1045/9	382 \pm 58	–	–

Table 4. Diameter ratios of the azimuthally averaged diameters of R Cas with respect to the 1045 nm/9 nm, 700 nm/6 nm and 671 nm/6 nm measurement. The diameters used are derived from fits of the fully darkened disk model (FDD) to the reconstructed visibilities.

Feature	FDD diameter ratio
(671/6)/(1045/9)	1.48 \pm 0.16
(700/6)/(1045/9)	1.26 \pm 0.14
(714/6)/(1045/9)	1.66 \pm 0.17
(671/6)/(700/6)	1.17 \pm 0.08
(714/6)/(700/6)	1.32 \pm 0.09
(714/6)/(671/6)	1.13 \pm 0.07

the diameters of Table 2 converted to linear radii (in solar radii R_{\odot}) using R Cas' HIPPARCOS parallax of 9.37 mas \pm 1.10 mas (Van Leeuwen et al. 1997).

The reconstructed images (Fig. 3) and visibilities reveal that R Cas has a significant elongation in the light of the strong TiO absorption bands (671 nm: PA=53°, axis ratio 0.70; 714 nm: PA=58°, axis ratio 0.76), and a slight elongation in the 700 nm moderate TiO absorption band (PA=54°, axis ratio 0.87). In the continuum at 1045 nm no elongation is visible (axis ratio >0.9). Table 2 shows that (i) the asymmetry (i.e. axis ratio) decreases with decreasing TiO absorption and (ii) the axis ratio is nearly independent of the artificial CLV. The peak intensity of the 671 nm and 714 nm images is not at the center. A discussion of the asymmetry of R Cas, including conceivable interpretations, may be found in Weigelt et al. (1996). The here observed decrease of the asymmetry with decreasing molecular band absorption, i.e. towards deeper layers, is consistent, e.g., with the dust disk scenario or may indicate temperature/density inhomogeneities in the upper layers where the strong TiO bands are formed.

Table 4 presents the ratios between the azimuthally averaged disk diameters of R Cas. We only list the FDD diameter ratios

Table 5. Properties of Mira model series (see text)

Series	Mode	P (days)	M/M_{\odot}	L/L_{\odot}	R_p/R_{\odot}	T_{eff}
D	f	330	1.0	3470	236	2900
E	o	328	1.0	6310	366	2700
P	f	332	1.0	3470	241	2860
M	f	332	1.2	3470	260	2750
O	o	320	2.0	5830	503	2250

since the FDD approximation provides reasonable fits to the CLV in near-continuum filters and many other filters (HS98, HSW98), and since UD and Gauss fits yield almost identical ratios. Note, however, that real diameter ratios can be different from those based on these artificial CLVs because, in particular, the shape of the physical CLV may be angle-dependent (e.g. occurrence of hot or cool spots). The ratios of artificial diameters show that the average diameter of R Cas is about 1.66 \times and 1.48 \times larger in the TiO strong-absorption band heads at 714 nm and 671 nm, respectively, than in the 1045 nm continuum. The average diameter at 700 nm (moderate TiO absorption band) is about 1.26 \times larger than at 1045 nm.

3. Comparison of the observations with Mira star models

In this section we compare our monochromatic radius observations with monochromatic radii predicted by Mira models. Since the wavelength dependence of the stellar radius sensitively depends on the structure of the Mira atmosphere (Bessell et al. 1989, BSW96, HSW98), this comparison should give some hint whether any of the models is a fair representation of R Cas. We also discuss the linear radii and the pulsation mode obtained by adopting R Cas's HIPPARCOS parallax and the effective temperature derived from the 1045/9 measurement and the bolometric flux.

All Mira star models used in this paper are from BSW96 (D and E series) and from HSW98 (P, M and O series). They are meant as possible representations of the prototype Mira variable o Ceti, and hence have periods P very close to the 332 day period of this star; they differ in pulsation mode, assumed mass M and assumed luminosity L ; and the BSW96 models differ from the (more advanced) HSW98 models with respect to the pulsation modelling technique. Solar abundances were assumed for all models. The five models represent stars pulsating in the fundamental mode (f ; D, P and M models) or in the first-overtone mode (o ; E and O models). Table 5 lists the properties of these Mira model series (R_p = Rosseland radius = distance from the “parent star's” center at which the Rosseland optical depth τ_{Ross} equals unity, $T_{\text{eff}} \propto (L/R_p^2)^{1/4}$ = effective temperature). We compare predictions of these models at different phases and cycles with our observations.

In this paper we use the conventional stellar radius definition where the monochromatic radius R_{λ} of a star at wavelength λ is given by the distance from the star's center at which the optical depth equals unity ($\tau_{\lambda} = 1$). In analogy, the photospheric stellar radius R is given by the distance from the star's center at which the Rosseland optical depth equals unity ($\tau_{\text{Ross}} = 1$).

Table 6. Link between the 27 abscissa values (model-phase combinations m) in Figs. 8 to 13, and the models. Additionally the variability phase ϕ_{vis} , the Rosseland radius R and the 1045 nm radius $R_{1045\text{nm}}$ in units of the parent star radius R_p , and the effective temperature $T_{\text{eff}}(R)$ associated to the Rosseland radius are given.

Model	ϕ_{vis}	R/R_p	R_{1045}/R_p	$T_{\text{eff}}(R)$	Abscissa
D27360	0+0.8	0.90	0.90	3050	1
D27520	1+0.0	1.04	1.04	3020	2
D27600	1+0.2	1.09	1.10	3010	3
D27760	1+0.5	0.91	0.90	2710	4
D28320	1+0.8	0.90	0.90	3050	5
D28760	2+0.0	1.04	1.05	3030	6
D28847	2+0.2	1.09	1.09	3000	7
D28960	2+0.5	0.91	0.90	2690	8
E8300	0+0.83	1.16	1.07	2330	9
E8380	1+0.0	1.09	1.09	2620	10
E8460	1+0.1	1.12	1.11	2760	11
E8560	1+0.21	1.17	1.15	2610	12
P71800	0+0.5	1.20	0.90	2160	13
P73200	1+0.0	1.03	1.04	3130	14
P73600	1+0.5	1.49	0.85	1930	15
P74200	2+0.0	1.04	1.04	3060	16
P74600	2+0.5	1.17	0.91	2200	17
P75800	3+0.0	1.13	1.14	3060	18
P76200	3+0.5	1.13	0.81	2270	19
P77000	4+0.0	1.17	1.16	2870	20
M96400	0+0.5	0.93	0.84	2310	21
M97600	1+0.0	1.19	1.18	2750	22
M97800	1+0.5	0.88	0.83	2460	23
M98800	2+0.0	1.23	1.20	2650	24
O64210	0+0.5	1.12	1.00	2050	25
O64530	0+0.8	0.93	0.91	2150	26
O64700	1+0.0	1.05	1.01	2310	27

This radius has the advantage of agreeing well (see Table 6 and the discussion in HSW98 for deviations sometimes occurring in very cool stars) with measurable near-infrared continuum radii and with the standard boundary radius of pulsation models with $T_{\text{eff}} \propto (L/R^2)^{1/4}$.

For each of our four filters (671/6, 700/6, 714/6 and 1045/9) we have calculated the theoretical CLVs corresponding to the above mentioned five Mira models at different phases and cycles. The stellar radius for filter transmission f_λ is the intensity and filter weighted radius

$$R_f = \frac{\int R_\lambda I_\lambda f_\lambda d\lambda}{\int I_\lambda f_\lambda d\lambda} \quad (1)$$

which we call stellar filter radius R_f after the definition of Scholz & Takeda (1987). In this equation R_λ denotes the above monochromatic $\tau_\lambda = 1$ radius, I_λ the central intensity spectrum and f_λ the transmission of the filter. Owing to the narrow widths of our filters the R_f radii are almost monochromatic $\tau_\lambda = 1$ radii if the molecular line structure of the TiO bands is neglected.

The observed stellar filter radius $R_{f,m}$ of R Cas corresponding to a certain filter f and model-phase combination m , was derived by a least-squares fit between the measured visibility and

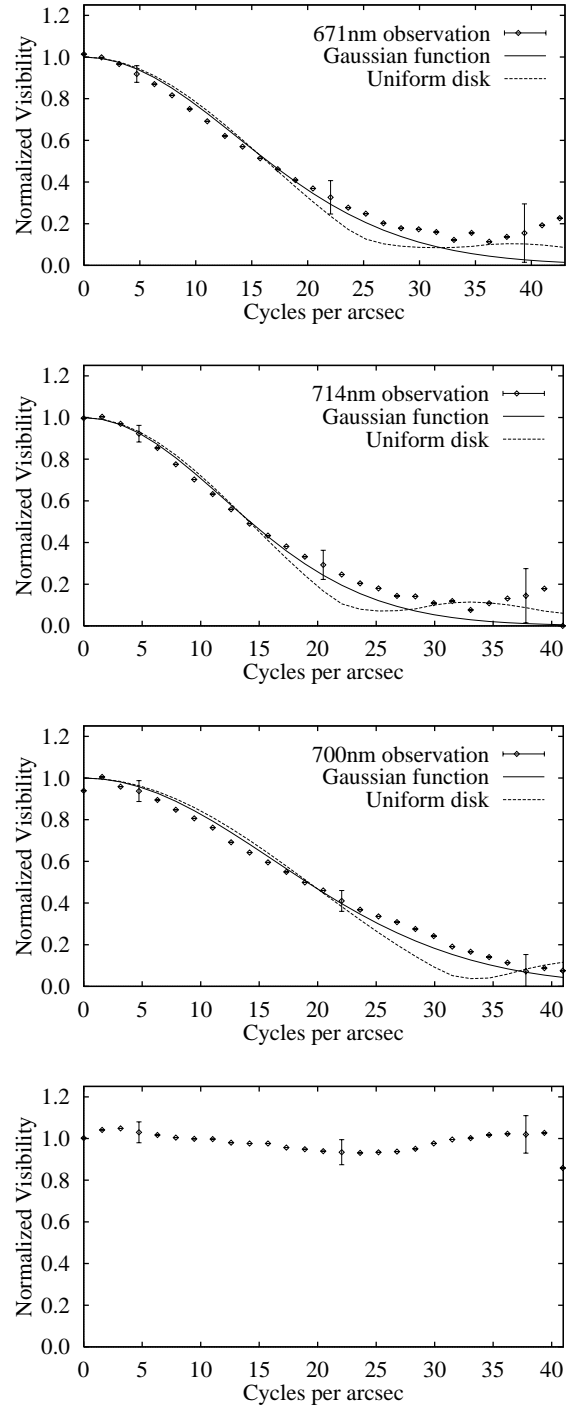


Fig. 4. Azimuthally averaged visibilities (dots) of R Cas, the unresolved star 51 And and of *elliptical* UD and Gaussian models with the same axis ratio as R Cas. From top to bottom: R Cas at 671 nm, 714 nm and 700 nm, and 51 And at 700 nm. The solid line corresponds to the best-fitting elliptical UD model, while the dashed line corresponds to the best-fitting elliptical Gaussian fit. The visibility data are plotted up to the telescope cut-off frequency (43.3, 41.3, and 40.6 cycles/arcsec for 671 nm, 700 nm, and 714 nm, respectively).

the visibility of the corresponding theoretical CLV. For illustration, examples of theoretical CLVs (filter 714/6 and 1045/9) are

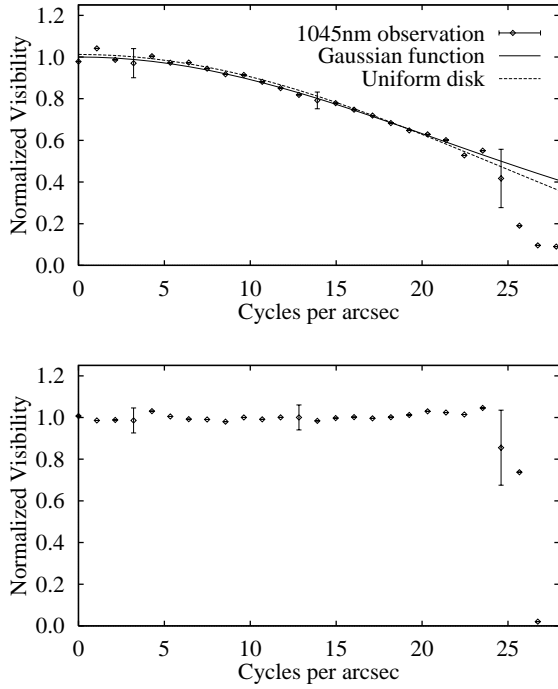


Fig. 5. Azimuthally averaged visibilities (dots) of R Cas (top) and of the unresolved star HIC 115022 (bottom; reference star was an independent data set of HIC 115022) at 1045 nm. The solid line is the best-fitting UD model, while the dashed line is a Gaussian fit. The visibility data are plotted up to the telescope cut-off frequency of 27.8 cycles/arcsec at 1045 nm.

presented in Fig. 6. For a detailed description of the visibility fitting procedure we refer to HS98. Because of the asymmetry discussed in Sect. 2.2, a 2-dimensional fit was applied: the theoretical 2-dimensional CLV was assumed to have an elliptical shape with a radial function equal to the theoretical 1-dimensional CLV. Since the applied Mira star models are spherically symmetric we have computed as stellar filter radius R_f the azimuthally averaged stellar filter radius R_f .

In the following subsections we apply CLVs predicted from all five models at phases both near our R Cas observations (phase 0.91 for filter 671/6, 700/6 and 714/6, and phase 0.63 for filter 1045/9) and, for comparison, also at other phases.

3.1. Comparison between observed and theoretical diameter ratios

We have compared the theoretical stellar filter radii $R_{f,m}^t$ as predicted by each model-phase combination m with our measured stellar filter radii $R_{f,m}$ by comparing the observed and theoretical diameter ratios at different wavelengths (filter f : 671/6, 700/6, 714/6 and 1045/9). By confronting a large variety of Mira models with the here presented narrow-bandpass observations, we may test how sensitively monochromatic radius measurements probe model structures and whether they are indeed reliable tools of Mira diagnostics. Since different models predict, at different phases, both different stellar filter radii R_f and different filter CLV curves, we expect better agreement between

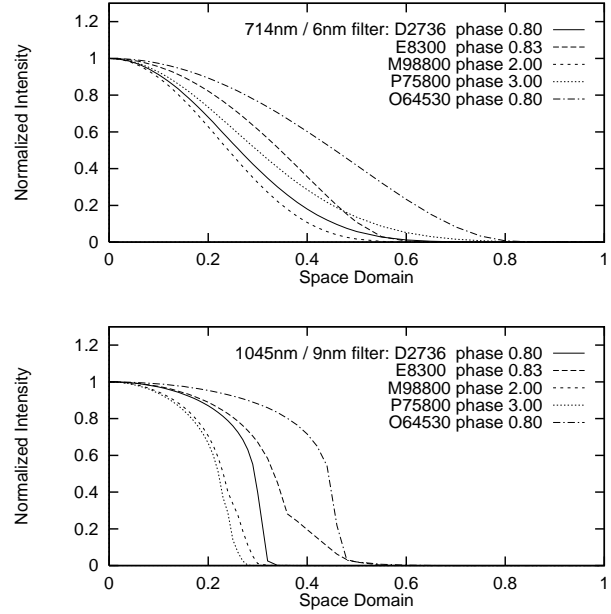


Fig. 6. Examples of theoretical center-to-limb variations for all five models and for phases close to our observations (from BSW96 and HSW98). The plotted CLVs are calculated for the 714/6 (top) and 1045/9 (bottom) filter.

model-predicted ratios and observed ratios (based upon the corresponding model-phase combination of CLV) for models that represent R Cas well and for model phases that are close to the observed phases than for other models and phases. We must be aware, however, (i) that none of our five models is specifically tailored to represent R Cas but rather *o* Cet, (ii) that model phases are close to but not identical with observed phases and cycle-to-cycle variations may be substantial (BSW96, HSW98), and (iii) that any spherically symmetric model star can at best provide an approximate description of the elongated (or spotted or partially obscured, cf. Weigelt et al. 1996) upper atmosphere of R Cas.

For illustration, Fig. 7 presents the observed and theoretical ratios R_f/R_{1045nm} of the stellar filter radii R_f and R_{1045nm} as a function of wavelength λ for all applied model series (D, E, P, M and O) and phases close to our observations (since nearly all model series consist of several cycles, a best fit selection was applied). Fig. 8 displays the observed and theoretical ratios for all model-phase combinations m and all filter pairs. Fig. 9 shows the distance D_m between the measured and theoretical stellar filter radius ratios. The distance D_m is defined as

$$D_m := \sqrt{\frac{\sum_{i \neq j}^{N_f} \left| \frac{R_{i,m}}{R_{j,m}} - \frac{R_{i,m}^t}{R_{j,m}^t} \right|^2}{\sum_{i \neq j}^{N_f} \left| \frac{R_{i,m}^t}{R_{j,m}^t} \right|^2}}, \quad (2)$$

where N_f is the number of filters used and the filter designation numbers i and j range between 1 and N_f (here: $N_f = 4$). The errors of the distances D_m were estimated according to the Gaussian error propagation law.

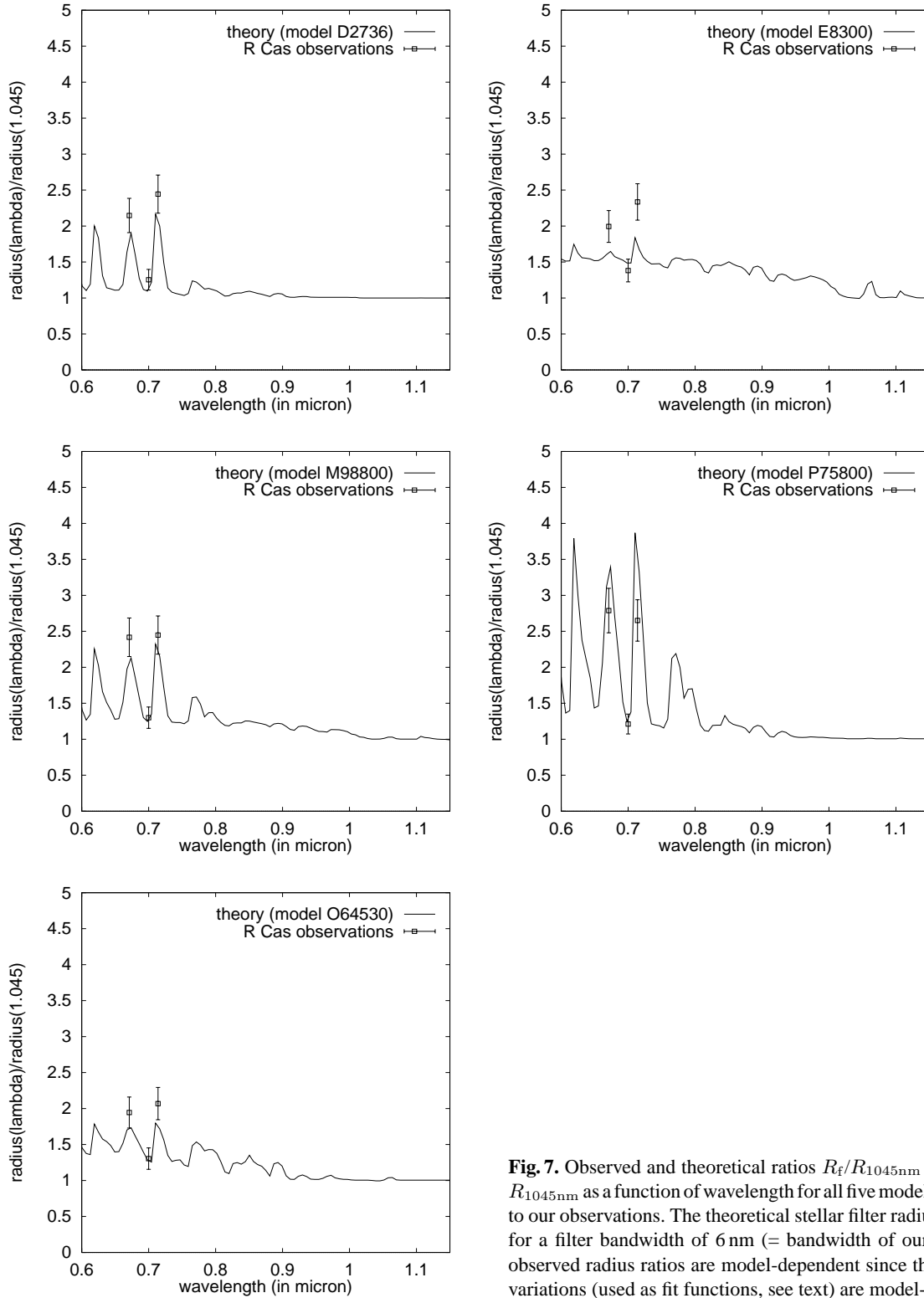


Fig. 7. Observed and theoretical ratios $R_f/R_{1045\text{nm}}$ of stellar filter radii R_f and $R_{1045\text{nm}}$ as a function of wavelength for all five models and for model phases close to our observations. The theoretical stellar filter radius curve $R_f(\lambda)$ is calculated for a filter bandwidth of 6 nm (= bandwidth of our optical filters). The above observed radius ratios are model-dependent since the theoretical center-to-limb variations (used as fit functions, see text) are model-dependent.

Note that the observations through the 3 optical filters were made at near-maximum phase (0.91) and the 1045 nm continuum observations at near-minimum phase (0.63). A correction of the 1045/9 angular diameters from phase 0.63 to 0.91 would imply increasing the diameter by roughly 0–30% depending on the model series (cf. Table 6). The diameter ratios in Fig. 8 con-

taining the 1045/9 observation will therefore be shifted downward by about 0 to 20%.

Inspection of Figs. 7, 8 and 9 shows that from the point of view of diameter ratios, some of the model-phase combinations are acceptable as representations of the here presented observations of R Cas but none is really satisfactory. Among the models

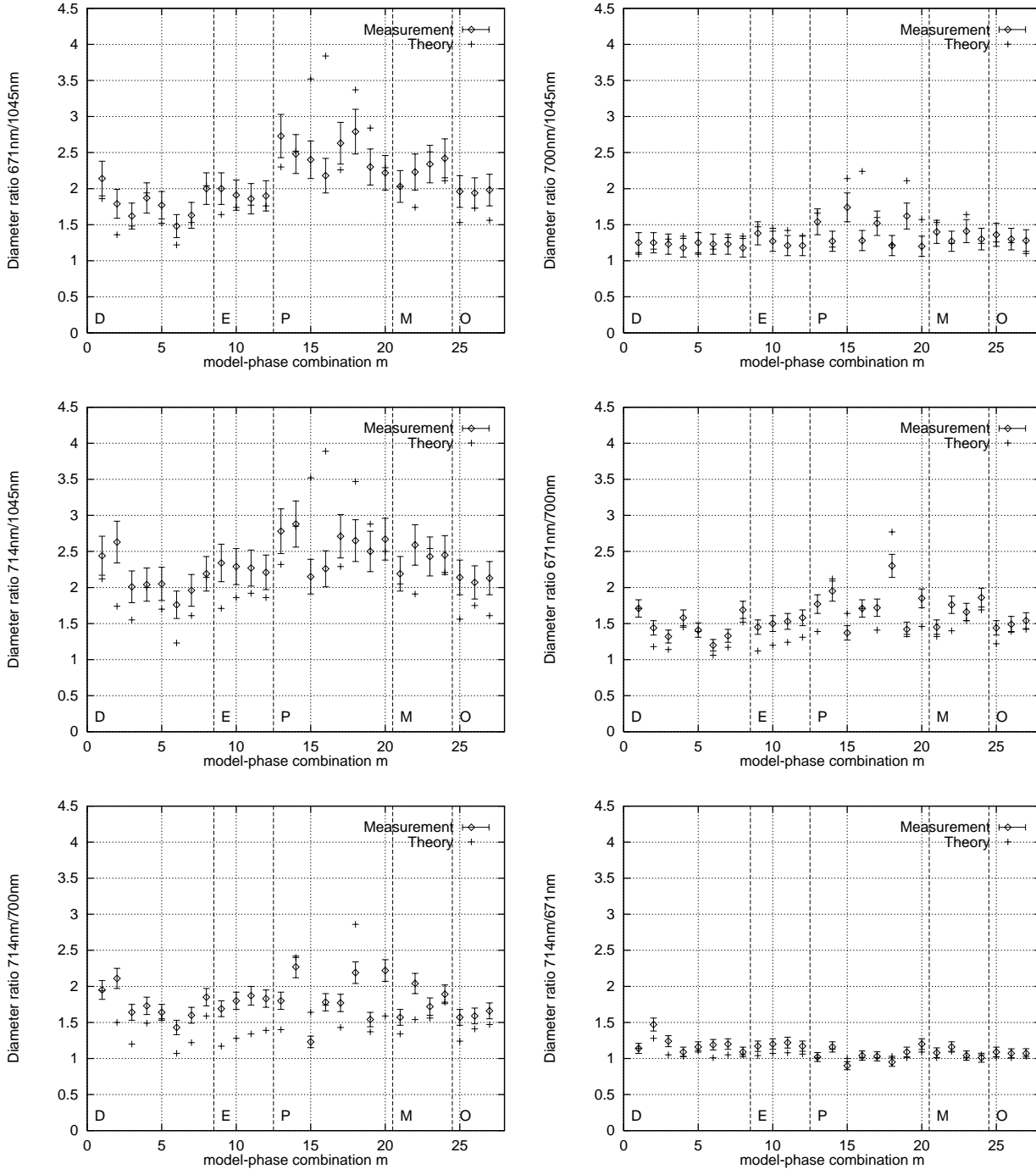


Fig. 8. Observed and theoretical ratios R_i/R_j of stellar filter radii R_i and R_j where i and j denote filters. The six plots show all possible filter combinations. Table 6 gives the link between the abscissa values and the models and their phases.

in the 0.8 to 1.0 phase range, only the phase 1.0 model of the P series just matches the observed phase 0.91 diameter ratios within the error bars. On the other hand, the Mira models predict the right order of TiO band to (near-) continuum diameters qualitatively quite well and much better than any static M giant models (HS98). Hence, monochromatic diameter observations involving wavelengths of different molecular band absorption are a promising technique of determining the stellar parameters of Mira variables.

3.2. Comparison of observed and theoretical linear radii

Linear stellar R Cas radii can be obtained if we use the new HIP-PARCOS parallax of R Cas of 9.37 ± 1.10 mas (Van Leeuwen et al. 1997; see discussion in this paper on the larger parallax errors in the case of stars with large extended shapes). The 1045 nm model CLV visibility was fitted to the measured 1045 nm visibility of R Cas yielding the monochromatic radius R_{1045} and, as predicted by the specific model, the associated Rosseland radius

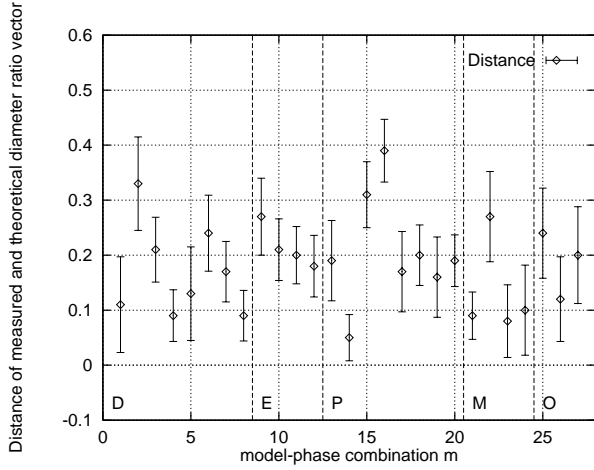


Fig. 9. Normalized distance D_m between the measured and theoretical diameter ratio vectors (see text). Table 6 gives the link between the abscissa values and the 27 model-phase combinations m .

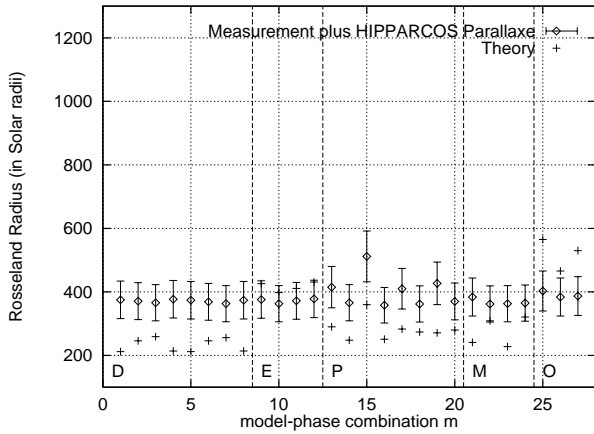


Fig. 10. Rosseland radii in R_\odot based on the 1045/9 measurements for each model/phase combination; Table 6 gives the link between the abscissa values and the models and their phases.

R (Fig. 10). We see that the derived Rosseland radius values are nearly the same for all model-phase combinations. The average measured R_{1045} radius is $359 \pm 58 R_\odot$ (31.3 ± 3.1 mas), and the average Rosseland radius is $377 \pm 60 R_\odot$ (32.9 ± 3.3 mas) (average over all model-phase combinations, peak-to-peak variation of about $70 R_\odot$ without the extreme value at model 15, i.e. P model at phase 1.5). The Rosseland radii of the E model series at all available phases (0.83, 1.0, 1.1, 1.21) and of the M model series at near-maximum phases (1.0, 2.0) are very close (i.e. within the error bars) to the Rosseland radii derived from the measured 1045 nm visibility, but the M model series is unsatisfactory when we look at near-minimum phases (0.5, 1.5) closer to our observed 0.63 phase. All other model-phase combinations yield large differences (larger than the error bars).

The theoretical 1045 nm continuum radius R_{1045} and the theoretical Rosseland radius R averaged over all available E model phases is $404 R_\odot$ and $416 R_\odot$, respectively, and the measured value (using the E model CLVs) is $361 \pm 58 R_\odot$ and

$372 \pm 60 R_\odot$, respectively. The E model at phase 0.83 closest to our observed phase 0.63 has $R_{1045} = 391 R_\odot$ ($R = 426 R_\odot$), and data reduction by means of this CLV yields for R Cas the observed value of $R_{1045} = 346 \pm 56 R_\odot$ ($R = 376 \pm 61 R_\odot$). Hence, the difference between model and star is smaller than the error bar.

For illustration, Fig. 11 presents the observed and theoretical stellar filter radii R_f in solar radii R_\odot as a function of wavelength for all five models and phases close to our observations (in the case of model series with several cycles the best fitting model is shown). In Fig. 12 we compare our observed linear stellar filter radii with the theoretical radii of all 27 model-phase combinations m . It is not surprising, yet impressive, how much more linear radii discriminate between models than relative radii as given in Figs. 7 and 8. Clearly the three fundamental-mode model stars are systematically too small (by ~ 20 to 40%), whereas most model radii of the overtone E and O series coincide within the error bars with the measured values. We see that the TiO forming layers of the Mira atmosphere may extend as far as 3 to 5 AU from the star's center.

3.3. Pulsation mode

Adopting the above phase-averaged linear Rosseland radius of $377 R_\odot \pm 60 R_\odot$ of R Cas, we find for the pulsation constant

$$Q = P (M/M_\odot)^{1/2} (R/R_\odot)^{-3/2} \quad (3)$$

a value of $Q = 0.059 \pm 0.013$ for a $1 M_\odot$ Mira with period $P = 430$ days. This Q value agrees well with the theoretical value ($Q = 0.056$) for first overtone pulsation mode for $1 M_\odot$ AGB stars with a period of ~ 430 days (Fox & Wood 1982, Wood 1990). The corresponding Q value of fundamental mode pulsation is $Q = 0.097$. Note, however, that no direct measurement of a Mira mass exists and that, e.g., a 20% uncertainty of M results in a 10% uncertainty of Q .

Van Leeuwen et al. (1997), referring to the Rosseland angular diameter of 24.9 mas measured by Haniff et al. (1995), give $286 R_\odot$ for the R Cas radius and suggest fundamental mode pulsation for this star from the period-radius relation. Inspection of the data of Haniff et al. shows that these authors measure a similar UD diameter (31.9 mas) in the 833 nm near-continuum filter as we do at 1045 nm (29.9 mas), but significant TiO contamination predicted by the E models for the 833 nm filter (cf. HSW98) leads to a smaller Rosseland diameter of 24.9 mas than our E model mean of 32.9 mas. Shifting R Cas upward in Fig. 1 of Van Leeuwen et al. to the here proposed radius position indicates first-overtone pulsation. We would expect that our value based on the direct 1045 nm continuum measurement is more realistic because corrections accounting for TiO band contamination may depend substantially on parameters and detailed properties of adopted models. Note, however, that the Haniff et al. and the present observations were obtained at different phases, namely near maximum and near minimum, respectively, and that typical Rosseland radius amplitudes are of the order of 10 to 20% (BSW96, HSW98). The appropriate cycle-averaged radius of R Cas (substituting for the non-observable parent star radius)

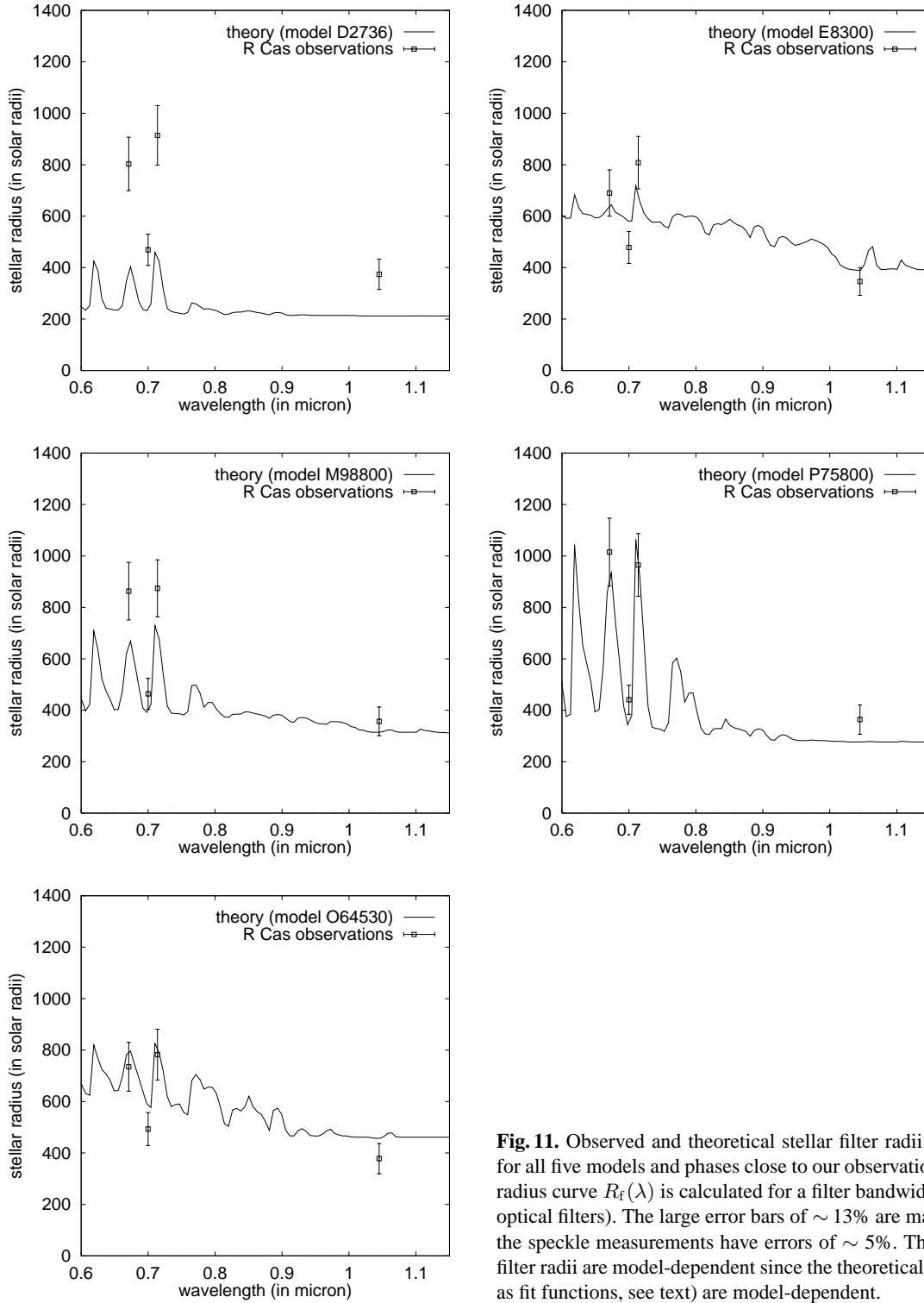


Fig. 11. Observed and theoretical stellar filter radii R_f in solar radii R_\odot versus λ for all five models and phases close to our observations. The theoretical stellar filter radius curve $R_f(\lambda)$ is calculated for a filter bandwidth of 6 nm (= bandwidth of our optical filters). The large error bars of $\sim 13\%$ are mainly due to the parallax error; the speckle measurements have errors of $\sim 5\%$. The above observed linear stellar filter radii are model-dependent since the theoretical center-to-limb variations (used as fit functions, see text) are model-dependent.

entering its Q value is not known yet. Regarding the UD diameter of only 13.55 mas quoted by Van Belle et al. (1996) and possible effects of overlooked absorption or scattering sources, we refer to Sect. 3.4. Note also that the period-luminosity relation favors fundamental pulsation for R Cas (Van Leeuwen et al. 1997, Bedding & Zijlstra 1998).

3.4. Effective temperature

The effective temperature of R Cas was derived by combining the angular photospheric diameter ($= 2 \times$ Rosseland radius derived from the 1045/9-observation with all above discussed models) with the bolometric flux using the relation

$$T_{\text{eff}} = 2341 \text{ K} \times (F_{\text{bol}}/\Phi^2)^{1/4} \quad (4)$$

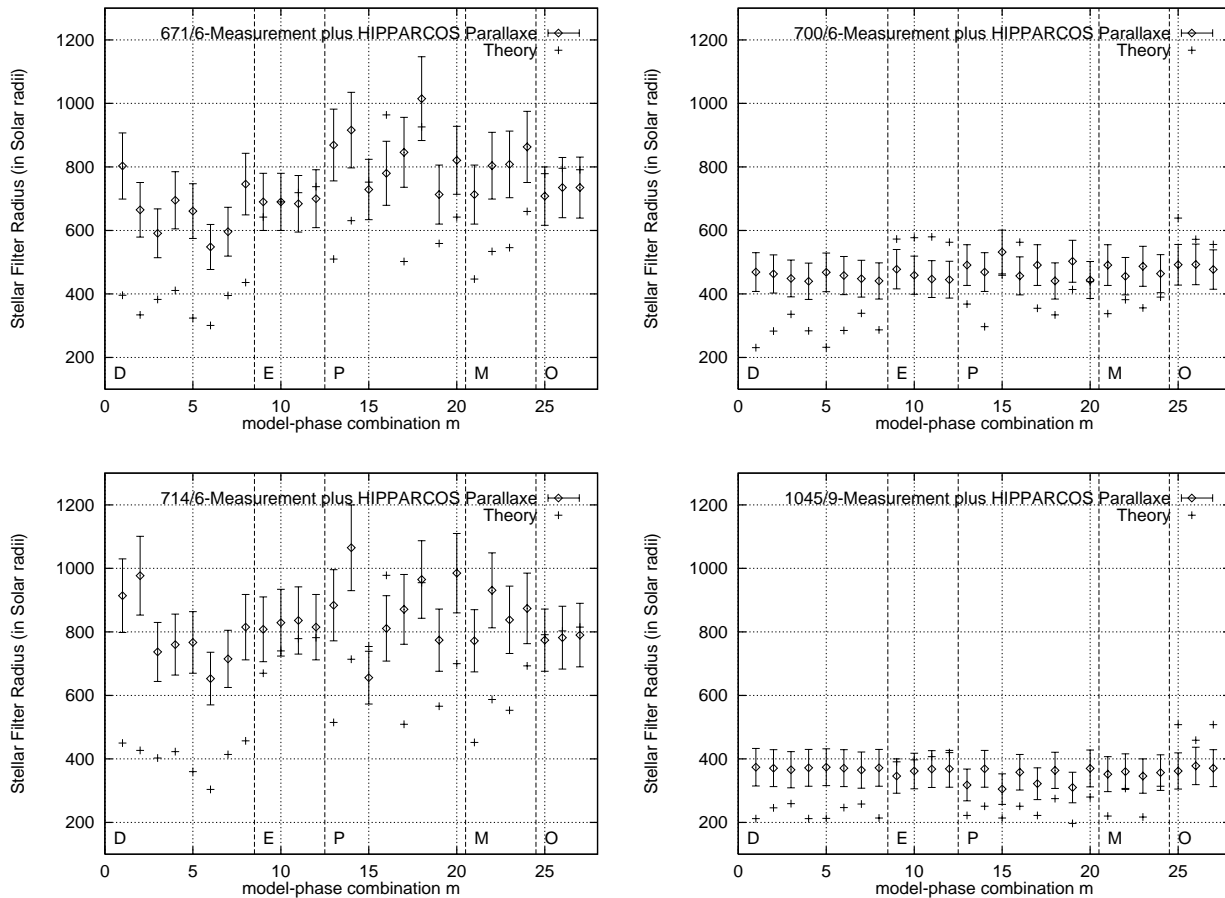


Fig. 12. Observed and theoretical stellar filter radii R_f in solar radii R_{\odot} for all 27 model-phase combinations m . The stellar filter radii R_f are given for the four filters 671/6 (top left), 700/6 (top right), 714/6 (bottom left) and 1045/9 (bottom right). Table 6 gives the link between the abscissa values and the models and their phases. The large error bars of $\sim 13\%$ are basically due to the parallaxe error; the speckle measurements have error bars of $\sim 5\%$.

where F_{bol} is the apparent bolometric flux in units of $10^{-8} \text{ erg cm}^{-2} \text{ s}^{-1}$ and Φ is the apparent angular photospheric diameter in mas. Fig. 13 (top) displays the angular Rosseland radii obtained from the 1045/9 observation by fitting all 27 theoretical model-phase CLV visibilities to the measured 1045/9 visibility. The average measured angular Rosseland radius is 16.4 mas (average over all model-phase combinations with the exception of the extreme value at position 15, i.e. P model at phase 1.5). Fig. 13 (top) also shows that inaccuracies caused by adopting incorrect continuum limb-darkening from inadequate models rarely exceed $\sim 10\%$ (i.e. 5% in T_{eff}).

For cool stars such as LPV's, where most of the luminosity is emitted at near-infrared wavelengths, a convenient method for calculating bolometric magnitudes is to use a blackbody function to interpolate between photometric measurements in the J, H, K and L bands. For estimating the bolometric flux we have used JHKL-flux measurements from B. Yudin's (1997, private communication) R Cas observations from August 1988 and September 1989. These observations were carried out at about the same variability phase (0.65–0.71) as our 1045/9 observation from October 1996 (0.63). The bolometric magnitude of R Cas, calculated by P. Whitelock

(1997, private communication) using B. Yudin's measurements, yields $m_{\text{bol}} = 1.99 \pm 0.20$ and, assuming that a zero magnitude star has a flux of $2795 \times 10^{-8} \text{ erg cm}^{-2} \text{ s}^{-1}$, yields $F_{\text{bol}} = 447.08 \times 10^{-8} \text{ erg cm}^{-2} \text{ s}^{-1}$. Fig. 13 (bottom) presents T_{eff} derived from each of the 27 model-phase combinations. Since we have the flux and the angular diameter of R Cas at the 1045/9 measurement for phase of ~ 0.6 only, the derived effective temperature values in Fig. 13 represent T_{eff} at near minimum phase (0.6) only. Fortunately, this value does little depend on the model-phase combination CLV and is about $1880 \pm 130 \text{ K}$ (average over all model-phase combinations with the exception of the extreme value at position 15, i.e. P model at phase 1.5). The peak-to-peak variation is about 160 K (without position 15). The closest E model with phase 0.83 has an effective temperature of 2330 K. Application of its CLV and $m_{\text{bol}} = 1.99 \pm 0.20$ (measured at phase ~ 0.6) to our 1045/9 observation yields for R Cas a Rosseland radius of 16.4 mas and an effective temperature of 1880 K (the same CLV with the phase-mean value of $m_{\text{bol}} = 1.1 \pm 0.2$ used in Hannif et al. 1995 yields an effective temperature of 2300 K).

Our 1045 nm measurement provides an important point in the effective temperature calibration of very late M giant spec-

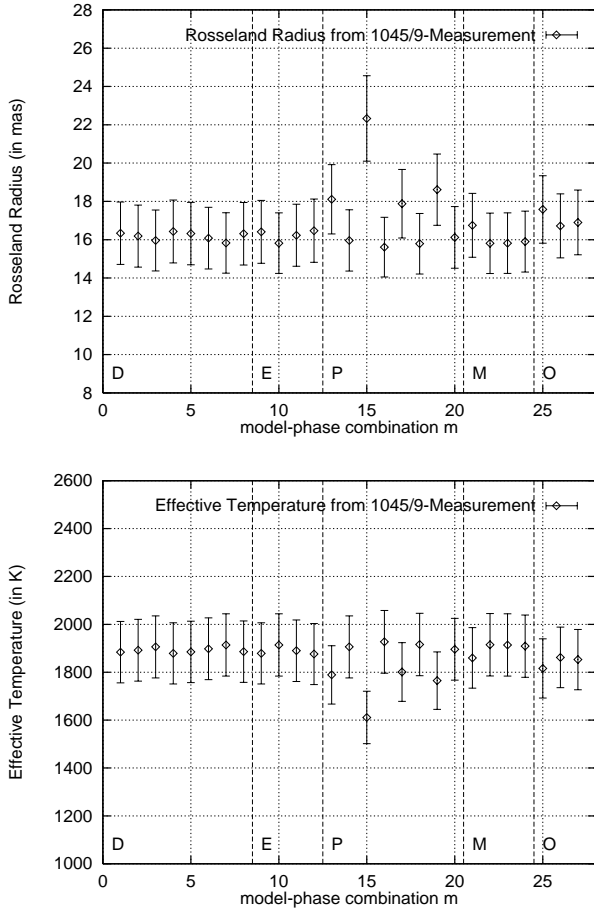


Fig. 13. Angular Rosseland radii (in mas) derived for each model-phase combination m from the 1045/9 measurements (top). Effective temperatures T_{eff} determined from the above angular Rosseland radii and the bolometric flux of R Cas measured around phase 0.6. Table 6 gives the link between the abscissa values and the models and their phases.

tral classes because R Cas at minimum phase *defines* the spectral type M10 in the standard classification scheme of Lockwood & Wing (1971) and Lockwood (1972), i.e. $T_{\text{eff}}(\text{M10}) \approx 1880 \pm 130$ K.

Van Belle et al. (1996) have also observed the continuum diameter ($\Phi_{UD} = 13.55$ mas at $2.2 \mu\text{m}$) and bolometric flux ($447.4 \cdot 10^{-8} \text{ erg cm}^{-2} \text{ s}^{-1}$) at phase 0.81 (still fairly close to the minimum in case of first-overtone pulsation as their M9.8 classification shows) and derive a surprisingly high effective temperature of 2954 ± 174 K for spectral type M9.8 (not included in their calibration Fig. 1). Their diameter is smaller than both our continuum value ($\Phi_{UD} = 29.9$ mas at 1045 nm) and the near-continuum value of Haniff et al. (1995) ($\Phi_{UD} = 30.8$ and 33.0 mas at 833 nm). It turned out in the meantime (G.T. Van Belle, private communication) that the entry 0.1245 of the visibility point in their Table 1 does possibly not belong to the central visibility lobe (as assumed) but to the first side maximum.

We propose $T_{\text{eff}} \approx 1900$ K for giants of spectral type M10 with an uncertainty of about 150 K assuming that no significant cycle-to-cycle variations occur.

Inspection of the static M giant models of Fluks et al. (1994) shows that these models account for additional near-infrared absorption, not included in the BSW96 and HSW98 models, also blanketing significantly the $1 \mu\text{m}$ region at non-Mira spectral types M8 to M10 ($T_{\text{eff}} = 2890$ K to 2500 K according to the authors). Since A. Lancon (private communication) observed similar flux depression at $1 \mu\text{m}$ in several late Miras, we cannot exclude that the $1 \mu\text{m}$ photons originate in noticeably higher layers than the continuum photons and that our measured radius has to be scaled to the continuum radius resulting in a smaller stellar radius and in a higher effective temperature. If, on the other hand, strong molecular line blanketing led to stronger limb darkening, the here given 1045 nm radius would have to be increased before downscaling to the continuum radius. Furthermore, molecular (or dust) scattering in high atmospheric layers as suggested by Perrin et al. (1999) might fake a larger photospheric diameter. Hence, the proposed value of $T_{\text{eff}} = 1900$ K at M10 still has to be regarded with due caution.

4. Discussion and conclusion

From our speckle observations of R Cas near maximum phase (0.93) we derive average UD diameters of 43.6 mas and 49.2 mas at the strong TiO absorption bands (through 671 nm/6 nm and 714 nm/6 nm filters, respectively) and 37.2 mas at the moderate TiO absorption band (700 nm/6 nm). In the continuum (1045 nm/9 nm) we find an UD diameter of 29.9 mas near minimum phase (0.63). R Cas has a significant asymmetry with position angle of roughly 55° . The asymmetry decreases (i.e. the axis ratio increases from 0.7 to ~ 1.0) with decreasing TiO absorption. This decrease of asymmetry with decreasing molecular band absorption, i.e. towards deeper layers, may indicate temperature/density inhomogeneities in the upper layers where the strong TiO bands are formed, but it is also consistent with a dust disk scenario as discussed by Weigelt et al. (1996).

Other high-resolution observations of R Cas were published by Haniff et al. (1995), and Tuthill et al. (1994). Haniff et al. have derived an average near-continuum UD diameter of 31.9 mas through their 833 nm/41 nm filter. Their observations in the moderate TiO absorption band (700 nm/10 nm filter) yield an UD diameter of 42.0 mas, and in the strong TiO absorption band (710 nm/10 nm filter) an UD diameter of 53.5 mas (these diameters are averaged over their measurements near maximum phase). Compared to our observations their derived diameters are about 2–5 mas larger which is within the error bars. A deviation from the circular symmetry in the moderate TiO absorption band is also reported by Tuthill et al. (1994) with a position angle of $\sim 0^\circ$ (July 1992).

When measured visibility data are reduced with limb-darkening predicted by recent Mira models (BSW96, HSW98), we find that strong-TiO $\tau_\lambda=1$ diameters depend substantially on the adopted model, whereas the continuum diameter does not. Since these models are spherically symmetric and are tailored to the parameters of α Ceti which has a shorter period and higher luminosity than R Cas, they must not be expected to predict quantitatively the properties of R Cas. The observed

714nm/1045nm diameter ratio is of the order of 2 to 3 which is larger than predicted by most models, and our value is in fact only matched by one near-maximum model of the P series of HSW98 which is a fundamental-mode pulsation series with strong cycle-to-cycle variations. In terms of the linear radius derived from our continuum diameter measurement and the HIPPARCOS parallax the first-overtone pulsation E series of BSW96 is close to R Cas though it is too hot and its atmosphere is too compact to provide a satisfactory representation of this star. We obtain a Rosseland $\tau_{\text{Ross}}=1$ radius of $R = 377 R_{\odot}$ with an accuracy of about 15% which, indeed, places R Cas among the overtone pulsators in the period-radius relation in contrast to the recent fundamental-mode claim of Van Leeuwen et al. (1997) based on a diameter measured in a TiO-contaminated near-continuum filter. Since, however, the period-luminosity relation rather indicates fundamental pulsation (Van Leeuwen et al. 1997, Bedding & Zijlstra 1998), the pulsation mode of R Cas remains an unsettled question.

Since the spectral subclass M10 is defined by the spectrum of R Cas at minimum, and since we have reliable measurements of both the continuum diameter and the flux near minimum phase, we obtained, as a by-product of this study, for the first time a safe T_{eff} calibration point, $T_{\text{eff}}(\text{M10}) = 1900 \pm 150 \text{ K}$, at the cool end of the temperature calibration of M giants. This value is in fair agreement with $\sim 2100 \text{ K}$ tentatively proposed by Richichi et al. (1999) from lunar occultation of RU Ari. Whether this point provides an extension of the general M giant calibration or whether there is a systematic offset between Miras and non-Miras is not quite clear at present (Van Belle et al. 1996, Richichi et al. 1999).

Acknowledgements. We thank Boris Yudin for sending us his JHKL photometric observations of R Cas, and Patricia Whitelock for calculating the bolometric flux of R Cas.

References

- Baier G., Weigelt G., 1983, A&A 121, 137
 Bedding T.R., Zijlstra A.A., 1998, ApJ 506, L47
 Bessell M.S., Brett J.M., Scholz M., Wood P.R., 1989, A&A 213, 209
 Bessell M.S., Scholz M., Wood P.R., 1996, A&A 307, 481 (BSW96)
 Bonneau D., Labeyrie A., 1973, ApJ 181, L1
 Bonneau D., Foy R., Blazit A., Labeyrie A., 1982, A&A 106, 235
 Fluks M.A., Plez B., Thé P.S., et al., 1994, A&AS 105, 311
 Fox M.W., Wood P.R., 1982, ApJ 259, 198
 Haniff C.A., Ghez A.M., Gorham P.W., et al., 1992, AJ 103, 1662
 Haniff C.A., Scholz M., Tuthill P.G., 1995, MNRAS 276, 640
 Hofmann K.-H., Scholz M., 1998, A&A 335, 637 (HS98)
 Hofmann K.-H., Weigelt G., 1986, A&A 167, L15
 Hofmann K.-H., Balega Y., Scholz M., Weigelt G., 1995a, In: Strassmeier K.G. (ed.) Stellar surface structure. IAU Symp. 176, Kluwer, Poster Proceedings, p. 45
 Hofmann K.-H., Seggewiss W., Weigelt G., 1995b, A&A 300, 403
 Hofmann K.-H., Scholz M., Wood P.R., 1998, A&A 339, 846 (HSW98)
 Karovska M., Nisenson P., Papaliolios C., Boyle R.P., 1991, ApJ 374, L51
 Labeyrie A., 1970, A&A 6, 85
 Labeyrie A., Koechlin L., Bonneau D., Blazit A., Foy R., 1977, ApJ 218, L75
 Lockwood G.W., 1972, ApJS 24, 375
 Lockwood G.W., Wing R.F., 1971, ApJ 169, 6
 Lohmann A.W., Weigelt G., Wirmitzer B., 1983, Appl. Opt. 22, 4028
 Pease F.G., 1931, Ergebn. Exacten Naturwiss. 10, 84
 Perrin G., Coudé du Foresto V., Ridgway S.T., et al., 1999, A&A 345, 221
 Quirrenbach A., Mozurkewich D., Armstrong J.T., et al., 1992, A&A 259, L19
 Richichi A., Fabbroni L., Ragland S., Scholz M., 1999, A&A 344, 511
 Scholz M., 1985, A&A 145, 251
 Scholz M., Takeda Y., 1987, A&A 186, 200 (erratum: 196, 342)
 Tuthill P.G., Haniff C.A., Baldwin J.E., 1994, In: Robertson J.G., Tango W.J. (eds.) Very high angular resolution imaging. IAU Symp. 158, Kluwer, Dordrecht, p. 395
 Van Belle G.T., Dyck H.M., Benson J.A., Lacasse M.G., 1996, AJ 112, 2147
 Van Leeuwen F., Feast M.W., Whitelock P.A., Yudin B., 1997, MNRAS 287, 955
 Von der Lühe O., 1984, J. Opt. Soc. Am. A. 1, 510
 Watanabe T., Kodaira K., 1979, PASJ 31, 61
 Weigelt G.P., 1977, Opt. Commun. 21, 55
 Weigelt G., Balega Y., Hofmann K.-H., Scholz M., 1996, A&A 316, L21
 Wilson R.W., Baldwin J.E., Buscher D.F., Werner P.J., 1992, MNRAS 257, 369
 Wood P.R., 1990, In: Caccari C., Clementini G. (eds.) Confrontation between stellar pulsation and evolution. ASP conference series 11, ASP, San Francisco, p. 355